AIAA SciTech Forum
6-10 January 2025, Orlando, FL
AIAA SCITECH 2025 Forum

10.2514/6.2025-1088

A Study of Elastic Deformation in Linkages

Charles C Gai* and Keith A Seffen
Advanced Structures Laboratory, Department of Civil Engineering
University of Cambridge, 7a JJ Thomson Ave, Cambridge, Cambridgeshire, United Kingdom, CB3 0FA

In this paper, we present a novel approach to mechanism design that integrates passive elastic deformation into the linkage framework, offering a balance between precision and adaptability. By leveraging on the difference in material properties between individual links, our methodology enables dynamic responses to external forces in certain specific configurations whilst maintaining reliability. Through theoretical analysis and physical experiments of a simple four-bar linkage mechanism, we validate our approach and pave the way for a new class of mechanism.

I. Nomenclature

L_i = Rest length of link i
S = Length of the shortest link for a four-bar linkage
L = Length of the longest link for a four-bar linkage
P, Q = Lengths of the intermediate links for a four-bar linkage
α = Input angle variable for a four-bar linkage
θ = Intermediate angle variable for a four-bar linkage
β = Output angle variable for a four-bar linkage
C = Compatibility equation for a rigid linkage motion
E_i = Young's modulus of link i
A_i = Cross-sectional area of link i
k_i = Spring stiffness of link i
p_i = Local coordinate system at mobile pin joints
$\varepsilon_{i,j}$ = Component of strain in link i in the direction of local coordinate j

II. Introduction

Linkage mechanisms play a critical role in a wide range of engineering applications, from origami modelling [1–4] and biomechanics [5–8], to robotics [9, 10] and aerospace deployable structures [11–13]. Traditionally, the design of these mechanisms has largely focused on rigid structures where all links and joints are assumed to be perfect and have no extension or deflection throughout the motion, aiming to achieve precise control over motion trajectories [14]. Such assumptions significantly simplify the design of linkage mechanism into purely geometrical problems; however, such designs often struggle to adapt to variations in operating conditions or accommodate for minor deviations in geometry, leading to inefficiencies and limitations in functionality.

On the other hand, compliant mechanisms offer a degree of flexibility by utilizing materials with inherent elasticity and incorporating flexible joint elements into the design [15]. These approaches allow for the design of mechanisms with a lower number of parts and a lower manufacturing difficulty. Although these mechanisms can adapt to changes in the environment or user inputs, they often sacrifice the possible range of motion its rigid linkage counterpart can achieve as well as precision and control [16]. Furthermore, the design and analysis of compliant mechanisms often require advanced computational tools such as FEA [17] and a deep understanding of material properties, making them more challenging to design compared to rigid linkages.

In this paper, we propose a novel approach to the design of linkage mechanisms that bridges the gap between rigid and compliant linkage systems. Our approach leverages on the passive elastic deformation of individual links to enable adaptive responses to external forces or perturbations whilst maintaining precise control over the majority of motion trajectories. This new class of linkage mechanism has the ability to switch between unique compatibility paths that

---

*Corresponding author email: ccg36@cam.ac.uk are inaccessible before without breaking and reconfiguring the mechanism entirely, similar to a bistable structure. By integrating material elasticity directly into the design process, we aim to unlock a diverse range of new possible applications of linkage mechanisms.

This study centers on the simplest yet most foundational planar linkage mechanism - the four-bar linkage - which serves as a critical building block for more complex linkages that can emerge through various tessellation strategies. In the following sections, we first present the fundamental key concepts and theoretical framework underlying our approach. Afterwards, we discuss the unique properties of such linkage mechanism along with experimental validation.

III. Initial Concepts

A. Compatbility paths

A linkage mechanism can be considered as a set of links and revolute pin joints that are connected to move in space under strain-free motion. Past research assumes that the links are rigid and that the joints are perfect, which enable a purely geometrical approach and simplify the motion analysis. In other words, the distance between two joints is always constant, which is equivalent to the length of the respective link L_i. In a two-dimensional (x, y) space, this can be expressed as:

$$\sqrt{(x_1 - x_2)^2 + (y_1 - y_2)^2} = L_i^2$$

where the joint coordinates are (x_1, y_1) and (x_2, y_2).

A typcial linkage system is a single degree-of-freedom mechanism moving in-plane. The corresponding compatbility path is formed by a set of points that describes the feasible positions of the mechanism where none of the links are strained. The exact path depends on the initial geometry of the mechanism and the length of the links — ultimately the postion of where the pin joints at their ends are located. For a simple four-bar planar linkage mechanism of rigid links and revolute joints only, the compatibility path can be derived through various methods such as the Freudenstein equation [18] or by directly considering the geometric compatibility condition for one of the links through the Pythagorean Theorem. For the four-bar linkage mechanism shown in Fig.1, we may write the compatibility path equation, C, as:

$$C = \sqrt{(L_{\text{fixed}} + L_3 \cos\beta - L_1 \cos\alpha)^2 + (L_3 \sin\beta - L_1 \sin\alpha)^2} - L_2 = 0; \tag{1}$$

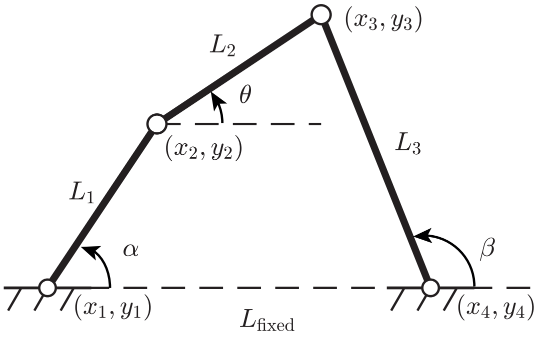

Fig. 1 Four-bar linkage notation.

It is clear from Eq.(1) that a different layout of the same topology of pin joints may result in significantly different compatibility paths whilst maintaining a single degree of freedom. These paths can be visualised instead as a set of curves in the (α, β) space, see Fig.2, where α and β are the inclination angles of the grounded links in Fig.1. These compatibility paths can be classified into different categories based on the Grashof theorem [19] and identifying where the shortest link is placed in the linkage system. The Grashof's theorem states that a four-bar mechanism has at least one revolving link (i.e. a crank exists) if:

$$S + L < P + Q$$

and no revolving link (i.e. all links are rockers) if:

$$S + L > P + Q$$

where S represents the length of the shortest bar, L represents length of the longest bar and P, Q are lengths of the intermediate bars. Table 1 summarises five possible cases of Grashof condition and its corresponding classification in more details.

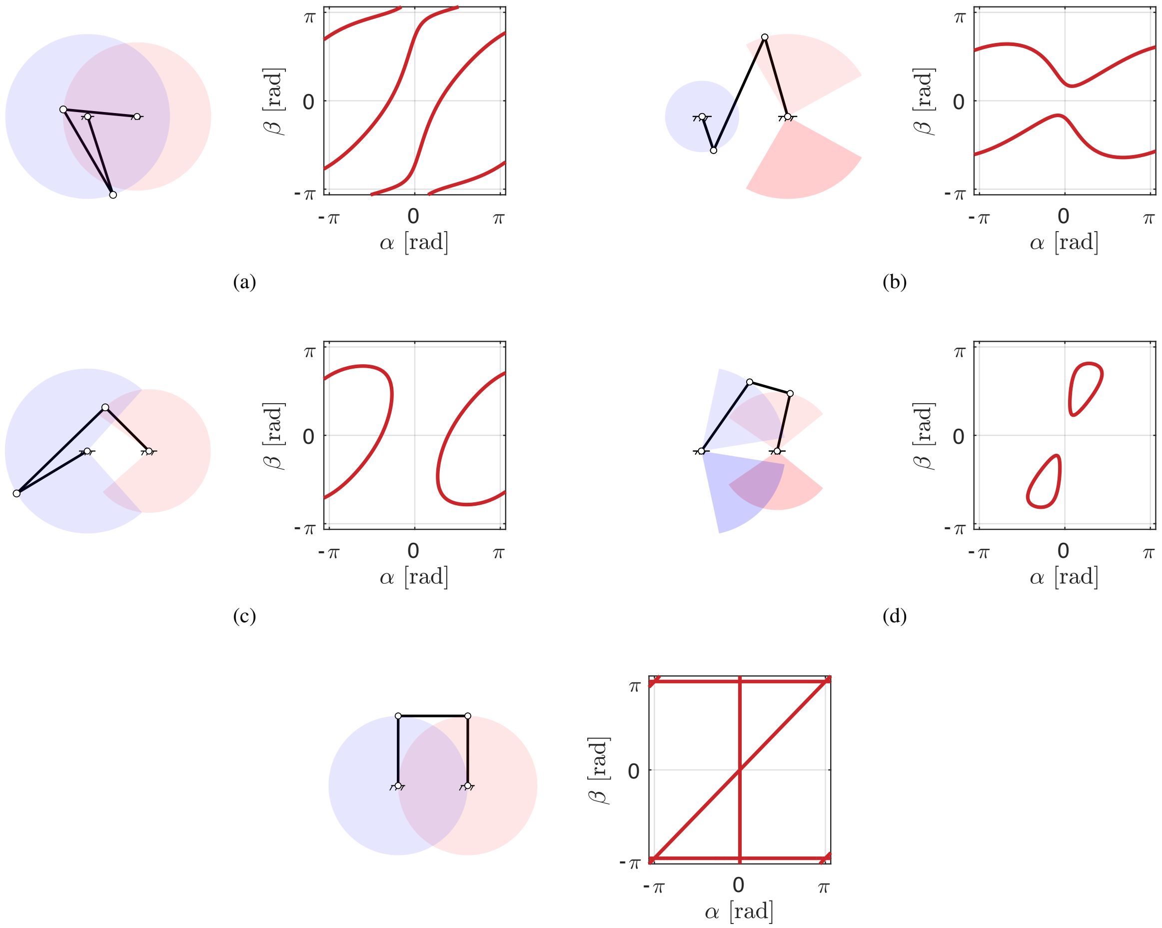

(a)

(b)

(c)

(d)

(e)

Fig. 2 Five different geometric configurations of four-bar linkage and its corresponding compatibility paths. Blue shaded area indicates the possible motion for angle α and red shaded area for angle β. Configuration (a), (b) and (d) all have two uniquely posible motion paths. Different shades of color in configruation (d) are correlated as a set of input and output. Configuration (e) has three bifurcation points where the motion path can switch from one path to the other.

Lengyel and Gáspár [20] first proposed a compatibility classification methodology for the linkage mechanism, which included bifurcation points and limit points. A bifurcation point represents a point on the compatibility path where the subsequent motion of the mechanism becomes indetermediate; the mechanism can instantaneously switch to a different motion path, which makes the system difficult to control precisely. On the other hand, a limit point is a distinct point on a compatibility path where one of the state variables (e.g. the rotating angles in Fig.1) is maximised or minimised in terms of the others. A limit point can also be seen as the point where a change in the driving angle parameter is necessary for the compatible motion to continue. If not, the motion can become "locked" at the limit point, behaving similarly to a rigid structure if the links are inextensible: see Fig.3. Past studies [21, 22] focus on the identification of these critical points, so that designers avoid undesirable behavior from happening.

Case	$L + S()P + Q$ **Relationship**	**Shortest link**	**Grashof Classification**
A	$<$	Ground (L_{fixed})	Double-crank
B	$<$	Ground-adjacent $(L_1$ or $L_3)$	Crank-rocker
C	$>$	Non-coupler link $(L_{\text{fixed}}, L_1$ or $L_3)$	Double-rocker
D	$>$	Coupler (L_2)	Triple-rocker
E	$=$	Any	Change point/ Bifurcation point

Table 1 Summary of all possible cases of Grashof condition and its corresponding classification

In this paper, we consider how to enable movement of the mechanism between different independent compatibility paths at these critical points by allowing for elastic stretching of links.

B. Classic Equilibrium Matrix Approach

Our investigation begins by examining the limit point configuration for four-bar linkage mechanisms. At a limit point, a conventional mechanism analysis assumes that the mechanism is completely fixed and rigid. If we plot a graph of torque applied on only the selected single angle variable, shown as Fig.4, we would expect to see a step change in force response from the linkage from zero to infinity as it approaches the "locked" state. A switch in the driving parameter variable resets the force response instantly back to zero. Previous studies [21, 23] have shown that at a limit point, the compatibility path equation C satisfies Eq.(2) with respect to the non-driving angle variable (referred to as the "dwelling" variable in the following discussion):

$$\frac{\partial C}{\partial \alpha} = 0 \quad \text{or} \quad \frac{\partial C}{\partial \beta} = 0 \tag{2}$$

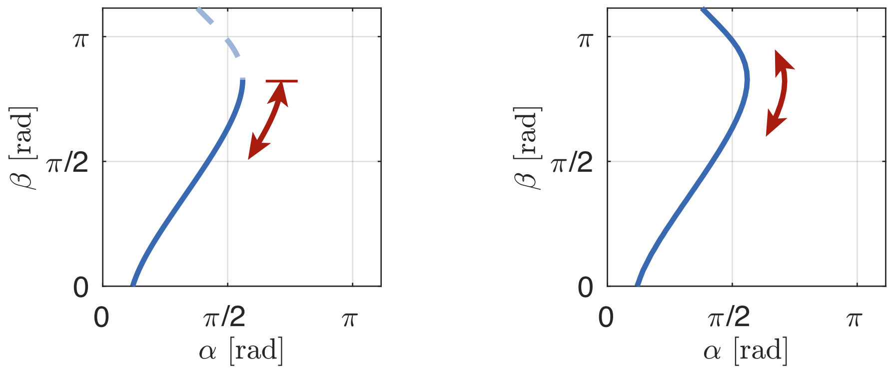

(a)

(b)

Fig. 3 Limit point as illustrated on a compatibility path: (a) shows the motion of the mechanism discontinues at the limit point where $\partial C/\partial \beta = 0$ if angle α is selected as the driving variable; (b) shows the motion of the mechanism continues freely as $\partial C/\partial \alpha \neq 0$ throughout if angle β is selected as the driving variable.

C. Mechanics of Solids Approach - Inclusion of Elastic Deformation

If we continue to exert an increasing torque or force in the direction of the driving variable whilst the linkage system is at a limit point configuration, the four-bar linkage shall deform if it is elastic. Therefore, we will assume that the system is an assembly of three separate, elastic bodies that are connected by perfect pin joints. When the links begin to deform elastically, the overall geometry of the linkage system changes and so does the prescribed compatibility path. We now enter a new domain where the system is no longer strain-free and the motion path is no longer prescribed;

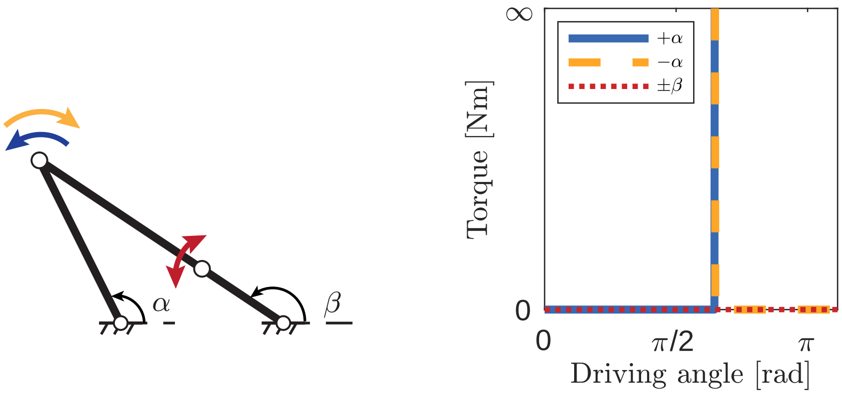

(a) (b)

Fig. 4 (a) A limit point configuration where $\partial C/\partial\beta = 0$. (b) The associated torque response for different driving variables as indicated by the colored arrows in (a) under traditional linkage analysis.

furthermore, the elastic system now engages large displacements whilst enduring relatively small strains in the material. The system is therefore under the influence of the external torque/forces and the material properties of the links.

In the following discussion, we examine deformation from the perspective of Solid Mechanics, deliberately beginning with more generalised principles to allow future extensions of the concept to more complex systems such as spatial linkages. In Solid Mechanics, the material deformation process is commonly described by a set of displacement vectors $\mathbf{u}$, strain tensor ε_{ij} and stress tensor σ_{ij} for points inside the solid body and Cartesian coordinates, q_i; If the body interacts with a surface, a traction vector $\mathbf{t}$ is also present. The linear elastic material properties can be described by the Young's modulus E and the Poisson's ratio ν, and they are valid for any point inside the body volume V or surface S. We may represent these relationships in their matrix form in Table 2:

			Component Notation	**Matrix Notation**
Kinematic equations	$\mathbf{u}-\boldsymbol{\varepsilon}$	in V	$\varepsilon_{ij}=\frac{1}{2}\left(\frac{\partial u_i}{\partial q_j}+\frac{\partial u_j}{\partial q_i}\right)$	$\varepsilon=\mathbf{D}\mathbf{u}$
Constitutive equations	$\boldsymbol{\varepsilon}-\mathbf{D}$	in V	$\sigma_{ij}=E_{ijkl}\varepsilon_{kl}$	$\sigma=\mathbf{E}\boldsymbol{\varepsilon}$
Equilibrium equations	$\sigma-\mathbf{b}$	in V	$\frac{\partial\sigma_{ij}}{\partial q_j}+b_i=0$	$\mathbf{D}^T\boldsymbol{\sigma}+\mathbf{b}=0$
Displacement boundary conditions	$\hat{\mathbf{u}}-\mathbf{u}$	on $S_{\hat{u}}$	$u_i=\hat{u}_i$	$\hat{\mathbf{u}}=\mathbf{u}$
Traction boundary conditions	$\sigma-\hat{\mathbf{t}}$	on $S_{\hat{t}}$	$\sigma_{ij}n_j=\hat{t}_i$	$\mathbf{P}_n\boldsymbol{\sigma}=\hat{\mathbf{t}}$

Table 2 Matrix formulation of fundamental equations in solid mechanics

Returning to our four-bar linkage system, the individual equilibrium equations for each link in the absence of body forces, such as gravitational force, are given by:

$$\frac{\partial}{\partial q_j}[C_{ijkl}\cdot\frac{1}{2}(\frac{\partial u_k}{\partial q_l}+\frac{\partial u_l}{\partial q_k})]=0 \tag{3}$$

The application of external force, $F_{i,\mathrm{ext}}$, to a mobile joint which connects m links, imposes the following boundary conditions on the system:

$$\sum_{i=1}^{m}F_x^{(i)}=F_{x,\mathrm{ext}} \quad \sum_{i=1}^{m}F_y^{(i)}=F_{y,\mathrm{ext}} \quad \sum_{i=1}^{m}F_z^{(i)}=F_{z,\mathrm{ext}} \tag{4}$$

where $F_x^{(i)}, F_y^{(i)}, F_z^{(i)}$ are the components of the internal force reacted at the pin joint by link i in the global coordinate (x, y, z) directions, respectively. For the purpose of this study, we shall make the following simplifying assumptions for the analysis of simple four-bar linkages:

- The material properties of the links can be modelled as axial, linear elastic springs ($\nu = 0$);
- The change in the cross-sectional area for all links is negligible ($\Delta A_i = 0$);
- There are no out-of-plane forces applied to the linkage and the deformation is constrained to the plane of the linkage; External forces are only applied at the mobile pin joints;
- Gravity force, hence body forces acting on the linkage are ignored;
- The revolute joints have no capacity to take moments and there is no separation within the joints;
- The traction condition is taken to be zero, $\mathbf{P}_n \boldsymbol{\sigma} = \hat{\mathbf{t}} = 0$ (i.e. on a smooth frictionless surface);
- Inertial effects are ignored.

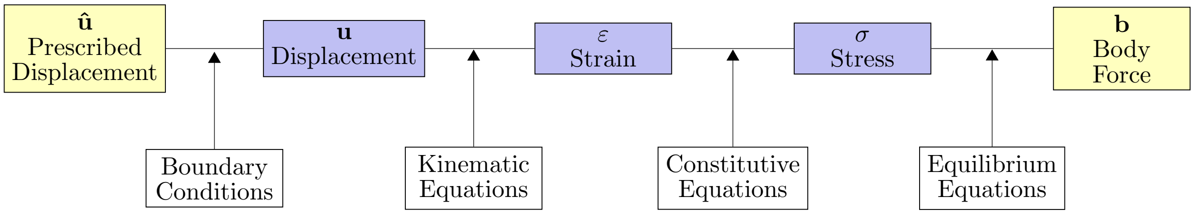

Fig. 5 Tonti diagram of the analytical model for a four-bar linkage system. Yellow blocks represent the input and output variables. Purple blocks represent the dependent variables calculated using the relationships outlined in the white blocks.

The stress-strain relationship for each individual link can therefore be written in the form of simple Hooke's Law:

$$\sigma_{11} = E_1 \varepsilon_{11}; \qquad \sigma_{22} = E_2 \varepsilon_{22} = 0; \qquad \sigma_{33} = E_3 \varepsilon_{33} = 0 \tag{5}$$

The global compatibility condition can now only be stated as the fixed distance between the two ground supports instead of individual links' rest length. For our four-bar linkage, this can be expressed in vector form:

$$\overrightarrow{L_1(1+\varepsilon_{L_1})} + \overrightarrow{L_2(1+\varepsilon_{L_2})} + \overrightarrow{L_3(1+\varepsilon_{L_3})} = \overrightarrow{L_{\text{fixed}}} \tag{6}$$

which decouples into two orthogonal compatibility equations:

$$L_1(1+\varepsilon_{L_1})\cos\alpha + L_2(1+\varepsilon_{L_2})\cos\theta - L_3(1+\varepsilon_{L_3})\cos\beta = L_{\text{fixed}} \tag{7a}$$

$$L_1(1+\varepsilon_{L_1})\sin\alpha + L_2(1+\varepsilon_{L_2})\sin\theta - L_3(1+\varepsilon_{L_3})\sin\beta = 0 \tag{7b}$$

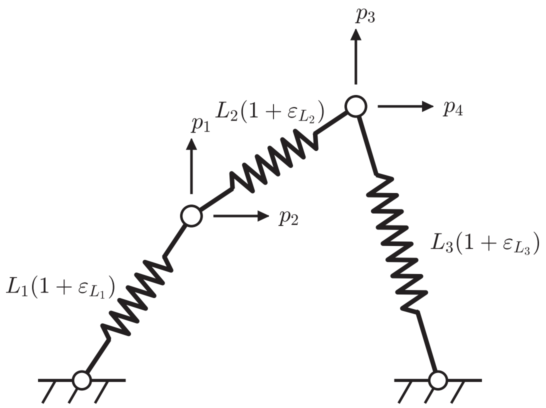

Fig. 6 Axial, linear elastic spring model of the four-bar linkage system and notations for local coordinate system.

For perfect pin joints, the three individual linear elastic links must satisfy the global compatibility conditions in Eq.(6) as a complete system as well as satisfying the local boundary conditions at each joint. For our axial springs and substituting for the stress-strain relationship in Eq.(5), we may write down an equivalent link stiffness k_i for each link i:

$$k_i = \frac{A_i E_i}{L_i} \tag{8}$$

We can then express the local joint equilibirum condition at each joint as:

$$\sum_{i=1}^{m} k_i L_i \varepsilon_{i,k} = F_k \tag{9}$$

where F_k is the total force acting in the direction of local position vector p_k on the joint; $\varepsilon_{i,k}$ represents the component of strain ε_i in the direction of p_k, and m are the number of links connected to the joint. We, thus, have four equations for our linkage:

$$k_{L_1} L_1 \varepsilon_{L_{1,1}} + k_{L_2} L_2 \varepsilon_{L_{2,1}} = F_1 \tag{10a}$$

$$k_{L_1} L_1 \varepsilon_{L_{1,2}} + k_{L_2} L_2 \varepsilon_{L_{2,2}} = F_2 \tag{10b}$$

$$k_{L_2} L_2 \varepsilon_{L_{2,3}} + k_{L_3} L_3 \varepsilon_{L_{3,3}} = F_3 \tag{10c}$$

$$k_{L_2} L_2 \varepsilon_{L_{2,4}} + k_{L_3} L_3 \varepsilon_{L_{3,4}} = F_4 \tag{10d}$$

It is clear that for a system with no strain or deformation in which the equilibrium conditions above are all satisfied, all forces acting on the joints must be zero. A compatible motion path can therefore be formed when all the strain terms are zero throughout the motion.

Alternatively, if all four force terms are non-zero and yet satisfying Eqs.(10), the linkage system will deform and be in equilibrium, behaving similarly to a rigid structure under a set of external loads. However, if we set only two out of the four force terms to be zero, another non-trivial equilibrium solution exists. For instance, let us set $F_3 = F_4 = 0$ – the system is in equilibrium if the following condition is satisfied:

$$k_{L_2} L_2 \varepsilon_{L_{2,3}} + k_{L_3} L_3 \varepsilon_{L_{3,3}} = 0$$

$$k_{L_2} L_2 \varepsilon_{L_{2,4}} + k_{L_3} L_3 \varepsilon_{L_{3,4}} = 0$$

The first solution recovers the rigid mechanism condition, where $\varepsilon_{L_2} = \varepsilon_{L_3} = 0$; the second solution, resembles a condition for a non-rigid mechanism to exist:

$$\frac{\varepsilon_{L_{2,3}}}{\varepsilon_{L_{3,3}}} = \frac{\varepsilon_{L_{2,4}}}{\varepsilon_{L_{3,4}}} = -\frac{k_{L_3} L_3}{k_{L_2} L_2} \tag{11}$$

Given the assumptions made, We can infer that the two links must remain collinear in order to satisfy Eq.(11) for a planar linkage:

$$\theta = \beta \tag{12}$$

Note that only the limit point configurations of the linkage on the rigid compatibility path satisfy Eq.(12). The traditional compatibility path equation, from a stress-strain equilibrium perspective, can also be interpreted as a "no-strain" condition for all of the links. The compatibility equation itself is written in the format where the coordinates of the nodes, for one of the links, are all in terms of the angle variables to simplify the analysis. For example, in Eq.(1), we are stating $L_2 \varepsilon_{L_2} = 0$ by expressing the position of end nodes of L_2 as a function of angle variable α and β and fixed length constant L_1, L_3 and L_{fixed}. Combining with Eq.(1) and Eq.(2), we may also state Eq.(11) in the form of:

$$\frac{\partial C}{\partial \beta} = \frac{\partial}{\partial \beta}(L_2 \varepsilon_{L_2}) = \frac{\partial}{\partial \beta}(\varepsilon_{L_3} \frac{k_{L_3} L_3}{k_{L_2}}) = 0 \tag{13}$$

Now, in this formulation, all three links can have a non-zero strain, reflecting the non-rigid behavior of the mechanism. A compatible non-rigid motion path can thus be computed, originating from the limit point configuration. This path defines a sequence of non-rigid configurations where the elastic extensions in the links evolve in a manner consistent with both the geometric compatibility and force equilibrium constraints.

The rermaining, non-zero force variables, F_1 and F_2, are input forces to the system, which act on the driving angle variable α. Different combinations of F_1 and F_2 of different magnitudes reflect various incident angles of the overall input force to the system. The value of strain in the links, and therefore the geometric configuration and motion path, depends directly on these force inputs. These forces dictate the deformation in the system by altering the equilibrium states. The interplay between F_1 and F_2 determines not only the magnitude and distribution of strains across the links but also influences the trajectory of the system's non-rigid motion.

Note that the local coordinate system p_i at each joint can be chosen and resolved independently: if the coordinates are chosen to be aligned with the input force instead of the global coordinate system, one of the force terms in the two remaining equilibrium equations is also zero. We can represent this modified local coordinate system as $p_{i,\mathrm{rot}}$, see Fig 7.

$$k_{L_1} L_{L_1} \varepsilon_{L_{1,1\mathrm{rot}}} + k_{L_2} L_2 \varepsilon_{L_{2,1\mathrm{rot}}} = 0 \tag{14}$$

$$k_{L_1} L_{L_1} \varepsilon_{L_{1,2\mathrm{rot}}} + k_{L_2} L_2 \varepsilon_{L_{2,2\mathrm{rot}}} = F \tag{15}$$

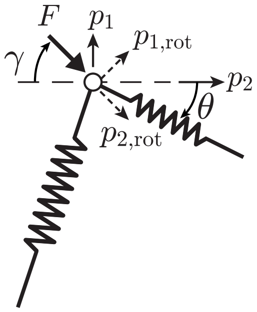

Fig. 7 Force inclination angle and rotated local coordinate system notation.

If a set of solutions exists for the system, we now have, in total, six independent system equations, Eqs.(7a), (7b), (11), (12), (14) and (15), with seven variables ($\varepsilon_{L_1}, \varepsilon_{L_2}, \varepsilon_{L_3}, F, \alpha, \theta$ and β). Furthermore, the force variable, F, only exists in one out of the six equations, Eq.(14). If the force inclination angle γ is fixed throughout the non-rigid motion, we may determine the non-rigid motion path in (α, β) space solely through the remaining five equations whilst ignoring the force variable F. In other words, the force response is decoupled from the derivation of kinematic motion path and can be determined later through Eq.(14).

IV. Four-Bar Linkage Example and Experimental Results

A. Example and Discussion

Let us illustrate this non-rigid motion path through a simple example utilising the previous assumptions. An experiment with LEGO Technic parts [24] has been crafted, with link L_2 modelled by a shock absorber and link L_1 and L_3 modelled by rigid standard beams made out of ABS (acrylonitrile butadiene styrene) at different length, see Fig.8.

We assume the rigid parts have the same cross-sectional area, i.e. $A_{L_1} = A_{L_3}$. The LEGO shock absorber part, which consists of a spring inside the cylinder, can be compressed easily and its stiffness is measured through an Instron test of force against displacement where $k_{2,c} = 0.3$ N/mm. Yet, the shock absorber has a similar magnitude of stiffness in tension as the other LEGO rigid beam parts. The stiffness of the other LEGO parts is estimated based on the material properties of ABS plastic with $k = EA/L$. Since the non-rigid link's stiffness in tension is significantly higher than it's stiffness in compression, we will assume that the system behaves as a rigid linkage mechanism outside of the compressive non-rigid path - even when the system operates at high angular velocity.

The material and geometric properties of the links used in the experiments are outlined in Table 3. The constructed linkage system here is a double rocker mechanism under the Grashof classification where none of the ground-adjacent link (link L_1 or L_3) can make a full revolution when chosen as the driving link.

Link	Rest Length (cm)	Stiffness in compression (N/mm)	LEGO Design ID
L_1	3.0	≈ 2100	42165
L_2	7.3	0.3	65151
L_3	3.2	≈ 2000	32316
L_{fixed}	5.6	∞ (Fixed length)	N/A

Table 3 Geometric and material properties of links in the four-bar linkage example. Stiffness in compression of the shock absorber (LEGO ID: 65151) is measured through an Instron test of force against displacement. Stiffness of the other links is estimated based on the material properties of ABS plastic where $E = 1.9$ GPa.

The revolute joints are recreated through standard LEGO pins with friction ridge (LEGO Design ID: 32062 and 2780). Two sets of experiments, one driven by a motor and the other by pulling a string, are performed to validate the theoretical analysis. In the string-pulling experiment, the string is pulled at a perpendicular direction to the driving link to drive the motion. In the motor driven experiment, the linkage system is connected to a motor that applies an anticlockwise torque on the input link L_1, i.e. increasing the angle variable α. Experimental data is only collected when a reasonable consistent kinematic motion is observed. The behavior of the system under this torque differs depending on the geometric design of the mechanism:

- If L_1 is designed as a crank (i.e., capable of a full revolution), the system will continue moving without interruption;
- If L_1 is designed as a rocker (i.e., restricted to a partial range of motion), the system behaves similar to a rigid linkage with continuous motion until it reaches the limit point configuration. At the limit point configuration, the driver link L_1 attempts to continue its motion, but the other two links become constrained.

When L_1 is a rocker, the torque τ applied by the motor can be seen as an equivalent force acting on the pin joint, aligning with our previous analysis through:

$$\tau = \vec{r} \times \vec{F}$$

where $\vec{r}$ is the position vector along the direction of L_1, with a magnitude of L_1, and $\vec{F}$ is the equivalent force acting at the pin joint connecting L_1 and L_2. By definition, $\vec{F}$ is always orthogonal to the direction of L_1 (i.e. an inclination angle $\gamma = \pi/2 - \alpha$).

When the non-rigid linkage reaches the limit point configuration, the applied torque τ induces deformation in the links, causing the system to follow the non-rigid motion path. If the applied torque is low, the resulting force $\vec{F}$ can be sufficiently balanced by the elastic restoring force of the deformed links. In this case, the mechanism settles into a static equilibrium along the non-rigid motion path, and the system remains in a strained, deformed configuration without further motion. However, if the torque exceeds the maximum threshold that the linkage can sustain whilst traversing the non-rigid motion path, the system will lose stability, snap into an alternative rigid compatibility path, and continue the kinematic motion until it reaches another limit point configuration.

A camera is used to capture the change in geometric position of the linkage. The strain in L_2 is calculated by examining individual photos taken by the camera throughout the motion in comparison to the rest length of the links in a static setup, see Fig.8(b). A selection of photos and the corresponding strain in link L_2 are shown in Fig.9.

Figure 10 illustrates both the analytical solution to the non-rigid motion path and the corresponding experimental results. In both experiments, the system successfully follows an alternative motion path without requiring a switch in the driving angle variable α, enabled by elastic compressive deformation in link L_2 as predicted. The good agreement between the two sets of experimental results implies that our simplified model, which neglects inertial effects, is sufficient for capturing the key mechanical behavior of the linkage system studied where the non-rigid link is only "non-rigid" in compression.

Nonetheless, it is crucial to acknowledge potential limitations of this model. Inertial effects may become significant in scenarios involving rapid torque variations or oscillatory forces, potentially altering the system's behavior in ways not captured by the our current quasi-static framework. Additionally, replacing the non-rigid link with one exhibiting significantly lower stiffness in both tension and compression than the other links could invalidate the present model. In such cases, the strain distribution across the links may no longer achieve static equilibrium as inertial effects become dominant, leading to a deviation from the predicted kinematic motion path and introducing complexities not addressed

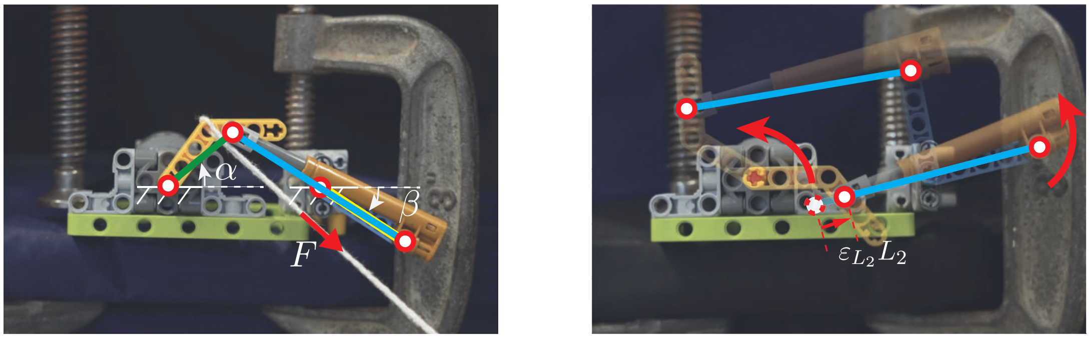

(a)

(b)

Fig. 8 Experimental setup and measurement of strain in link L_2. (a) String-pulling experimental setup. Notations of angles and links represented. (b) Motor-driven experimental setup. Observation and measurement of strain in link L_2 during the motion.

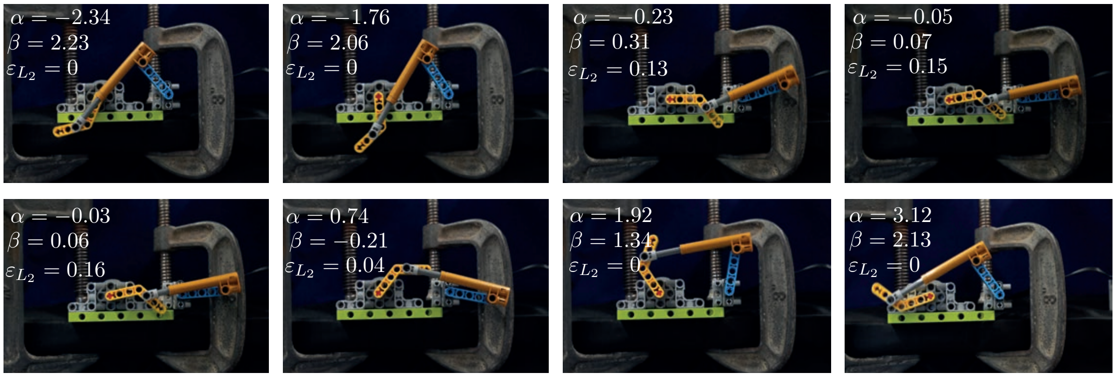

Fig. 9 Experimental results showing the non-rigid motion path observed and its corresponding strain in link L_2.

by the simplified assumptions.

Future investigations should examine the boundary conditions under which these quasi-static assumptions break down and explore the implications of altered stiffness profiles. Such studies would provide deeper insights into the dynamic behavior of the linkage and help refine the model for broader applicability.

Coming back to our experimental results, the main discrepancy between our theory and the experimental result lies in the region $(\alpha, \beta) \approx (0, 0)$, the unstable equilibrium configuration where all links become collinear, and $(\alpha, \beta) \approx (0.8, -0.6)$, the limit point configuration. In theory, when the linkage follows the non-rigid motion path and reaches the alternative compatibility path, it first arrives at the limit point on the alternative compatibility path, which now becomes a bifurcation point. Subsequent motion may be indeterminate – an increment in the driving variable, α, can yield two possible motions in output variable, β. However, the experimental result shows a deviation from such prediction. After examining the relevant strain response of ε_{L_2} and overall force response illustrated in Fig.10(c), it is clear that this discrepancy stems from the instability post snap-through.

After the maximum force threshold is passed, the linkage system will continue to move in accordance with the theoretical prediction until it reaches the unstable equilibirum position, $(\alpha, \beta) = (0, 0)$, where the local energy maxima of the system is located. In other words, the configuration with maximum strain in each of the three links. Any small perturbation in either angle variable, α or β, along will cause the system to immediately move to the next stable configuration – an arbitary point on the rigid compatibility path. The subsequent motion is likely to be affected by various factors such as the inertia, momentum and friction within the joints.

The general shape of force response for our non-rigid motion path in between the two limit points is very similar to an ordinary snap-through buckling response in a pin-jointed arch, also known as von Mises truss, which exhibits a diminishing stiffness response as the input force increases. When the overall stiffness of the structure reaches zero, the

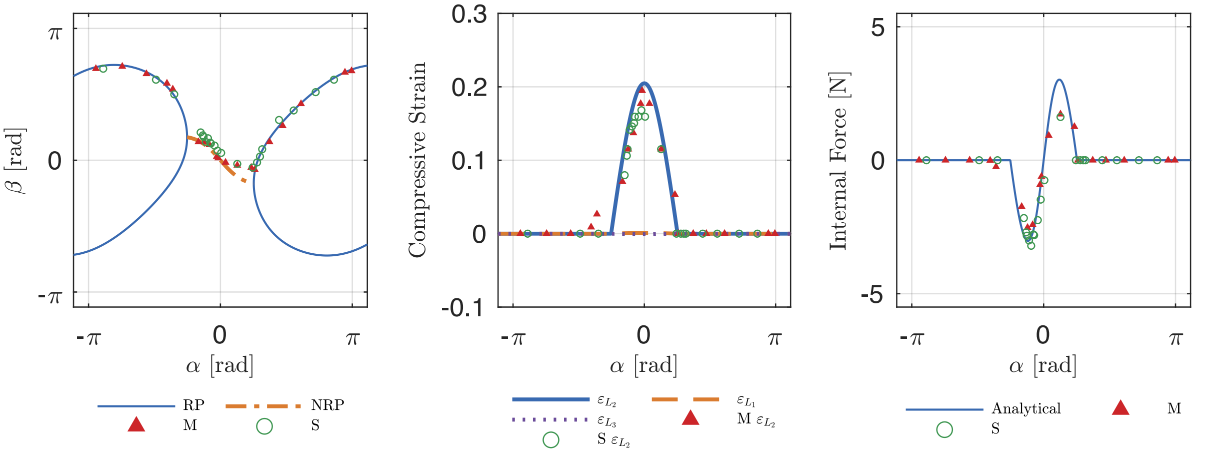

(a) (b) (c)

Fig. 10 RP = Rigid Path, NRP = Non-Rigid Path, M = Motor Experiment, S = String-pulling Experiment. (a) Motion paths shown in (α, β) space with an increasing driving variable α. (b) Strain variation in all three links. (c) Force response of L_2 at the pin joint between L_1 and L_2 in the direction of $p_{2,\text{rot}}$. Positive force is taken to be in the positive direction of $p_{2,\text{rot}}$.

structure will buckle and snap into a new stable position. The force response will then subsequently increase again as the structure is further deformed from the newly reached stable position. Unlike the Von Mises truss, where at a crticial load the sudden change in geometric position will bring the structure to an another deformed stable state, the linkage system will immediately return to the a strain-free rigid compatible motion path once the critical load threshold is passed. All the elastic energy stored in the system during the deformation process is released and converted into kinetic energy.

V. Conclusion

We have solved analytically for the non-rigid motion path of a four-bar linkage for a generic set of geometric parameters and linear elastic material properties, accurately predicting the motion trajectory, snap-through threshold, and strain in each link. A simple experiment was conducted for verification. The results show that the non-rigid motion path can be achieved by allowing for elastic deformation in one or more of the links; and the system can take a different continuous path without having to switch the driving parameter variable.

Future work will focus on extending this analysis to more complex linkage systems such as six-bar linkages and exploring the potential for practical applications in engineering and structural design.

References

[1] Filipov, E. T., Liu, K., Tachi, T., Schenk, M., and Paulino, G. H., “Bar and hinge models for scalable analysis of origami,” *International Journal of Solids and Structures*, Vol. 124, 2017, pp. 26–45. https://doi.org/10.1016/J.IJSOLSTR.2017.05.028.

[2] Meloni, M., Cai, J., Zhang, Q., Lee, D. S.-H., Li, M., Ma, R., Parashkevov, T. E., and Feng, J., “Engineering Origami: A Comprehensive Review of Recent Applications, Design Methods, and Tools,” , 7 2021. https://doi.org/10.1002/advs.202000636.

[3] Wang, C., Zhang, D., Li, J., and You, Z., “Kirigami-inspired thick-panel deployable structures,” *International Journal of Solids and Structures*, Vol. 251, 2022. https://doi.org/10.1016/j.ijsolstr.2022.111752.

[4] Chen, Y., Peng, R., and You, Z., “Origami of thick panels,” *Science*, Vol. 349, 2015, pp. 396–400. https://doi.org/10.1126/science.aab2870, URL https://www.science.org/doi/abs/10.1126/science.aab2870.

[5] Faber, J. A., Arrieta, A. F., and Studart, A. R., “Bioinspired spring origami,” *Science*, Vol. 359, 2018, pp. 1386–1391. https://doi.org/10.1126/SCIENCE.AAP7753, URL https://www.science.org.

[6] Mintchev, S., Shintake, J., and Floreano, D., “Bioinspired dual-stiffness origami,” , 2018. URL https://www.science.org.

[7] Baek, S.-M., Yim, S., Chae, S.-H., Lee, D.-Y., and Cho, K.-J., "Ladybird beetle-inspired compliant origami," , 2020. URL https://www.science.org.

[8] Seymour, K., Sheffield, J., Magleby, S. P., and Howell, L. L., "Cylindrical Developable Mechanisms for Minimally Invasive Surgical Instruments," 2019, p. V05BT07A054. https://doi.org/10.1115/DETC2019-97202, URL https://doi.org/10.1115/DETC2019-97202.

[9] Wu, S., Ze, Q., Dai, J., Udipi, N., Paulino, G. H., and Zhao, R., "Stretchable origami robotic arm with omnidirectional bending and twisting," *Proceedings of the National Academy of Sciences of the United States of America*, Vol. 118, 2021. https://doi.org/10.1073/pnas.2110023118.

[10] Kotikian, A., McMahan, C., Davidson, E. C., Muhammad, J. M., Weeks, R. D., Daraio, C., and Lewis, J. A., "Untethered soft robotic matter with passive control of shape morphing and propulsion," *Science Robotics*, Vol. 4, 2019, p. 7044. https://doi.org/10.1126/SCIROBOTICS.AAX7044, URL https://www.science.org.

[11] You, Z., and Pellegrino, S., "Cable-stiffened pantographic deployable structures part 1: Triangular mast," *AIAA Journal*, Vol. 34, 1996, pp. 813–820. https://doi.org/10.2514/3.13144.

[12] Chen, Y., You, Z., and Tarnai, T., "Threefold-symmetric Bricard linkages for deployable structures," *International Journal of Solids and Structures*, Vol. 42, 2005, pp. 2287–2301. https://doi.org/10.1016/j.ijsolstr.2004.09.014.

[13] Chen, Y., and You, Z., "Square deployable frames for space applications. Part 2: Realization," *Proceedings of the Institution of Mechanical Engineers, Part G: Journal of Aerospace Engineering*, Vol. 221, 2007, pp. 37–45. https://doi.org/10.1243/09544100JAERO100.

[14] Hunt, K. H., *Kinematic Geometry of Mechanisms*, 1st ed., Clarendon Press, 1978.

[15] Brown, N., Ynchausti, C., Lytle, A., Howell, L. L., and Magleby, S. P., "Approaches for Minimizing Joints in Single-Degree-of-Freedom Origami-Based Mechanisms," *Journal of Mechanical Design*, 2022, pp. 1–17. https://doi.org/10.1115/1.4054633.

[16] Kota, S., Joo, J., Li, Z., Rodgers, S. M., and Sniegowski, J., "Design of Compliant Mechanisms: Applications to MEMS," , 2001.

[17] Parlaktaş, V., Tanık, E., and Çağıl Merve Tanık, "On the design of a novel fully compliant spherical four-bar mechanism," *Advances in Mechanical Engineering*, Vol. 11, 2019. https://doi.org/10.1177/1687814019879548.

[18] Freudenstein, F., "Approximate synthesis of four-bar linkages," *Resonance*, Vol. 15, 2010, pp. 740–767. https://doi.org/10.1007/s12045-010-0084-7, URL https://doi.org/10.1007/s12045-010-0084-7.

[19] Grashof, F., *Theoretische Maschinenlehre: Theorie der Getriebe und der mechanischen Meßinstrumente. 2*, Vol. 2, Voss, 1883.

[20] Lengyel, A., and Gáspár, Z., "Classification of compatibility paths of SDOF mechanisms," *International Journal of Solids and Structures*, Vol. 42, 2005, pp. 21–36. https://doi.org/10.1016/j.ijsolstr.2004.07.005.

[21] Lengyel, A., and You, Z., "Analogy between bifurcations in stability of structures and kinematics of mechanisms," *Mechanics Based Design of Structures and Machines*, Vol. 31, 2003, pp. 491–507. https://doi.org/10.1081/SME-120023168.

[22] Lengyel, A., and You, Z., "Bifurcations of SDOF mechanisms using catastrophe theory," *International Journal of Solids and Structures*, Vol. 41, 2004, pp. 559–568. https://doi.org/10.1016/j.ijsolstr.2003.09.024.

[23] Tarnai, T., *Kinematic Bifurcation*, Springer Vienna, 2001, pp. 143–169. https://doi.org/10.1007/978-3-7091-2584-7_8, URL https://doi.org/10.1007/978-3-7091-2584-7_8.

[24] LEGO, "LEGO Pick A Brick," , 2024. URL https://www.lego.com/en-gb/pick-and-build/pick-a-brick.